# Global stability of 180°-bend pipe flow with mesh adaptivity

Daniele Massaro [1,*] Valerio Lupi [1] Adam Peplinski [1] and Philipp Schlatter [1,2]

[1] *SimEx/FLOW, Engineering Mechanics, KTH Royal Institute of Technology, Stockholm 100 44, Sweden*

[2] *Institute of Fluid Mechanics (LSTM), Friedrich–Alexander–Universität Erlangen–Nürnberg (FAU), Erlangen 91058, Germany*

(Received 9 June 2023; accepted 25 October 2023; published 20 November 2023)

The global stability of the flow in a spatially developing 180°-bend pipe with curvature $\delta = R/R_c = 1/3$ is investigated by performing direct numerical simulations to understand the underlying transitional mechanism. A unique application of the adaptive mesh refinement technique is used during the stability analysis for minimizing the interpolation and quadrature errors. Independent meshes are created for the direct and adjoint solutions, as well as for the base flow extracted via selective frequency damping. The spectrum of the linearized Navier-Stokes operator reveals a pair of complex conjugate eigenvalues, with frequency $f \approx 0.233$. Therefore, the transition is attributed to a Hopf bifurcation that takes place at $\mathrm{Re}_{b,\mathrm{cr}} = 2528$. A structural sensitivity analysis is performed by extracting the wavemaker. We identify the primary source of instability located on the outer wall, $\theta \approx 15°$ downstream of the bend inlet. This region corresponds to the separation bubble on the outer wall. We thus conclude that the instability is caused by the strong shear resulting from the backflow, similar to the 90°-bend pipe flow. We believe that understanding the stability mechanism and characterizing the base flow in bent pipes is crucial for studying various biological flows, like blood vessels. Hence, this paper aims to close the knowledge gap between a 90°-bend and toroidal pipes by investigating the transition nature in a 180°-bend pipe flow.

DOI: 10.1103/PhysRevFluids.8.113903

## I. INTRODUCTION

The flow in bent pipes serves as a valuable framework in various biological and technical scenarios, including the aortic arch that exits from the left ventricle of the heart and piping systems in process engineering. Differently from straight pipes, in the curved section, the centrifugal force pushes the flow towards the outer region and is balanced by a pressure gradient from the outer to the inner surface. This causes a secondary flow pattern which consists of a pair of symmetric, counterrotating vortices, named Dean vortices. They are Prandtl's first kind of secondary motion occurring perpendicular to the main flow direction and present in both laminar and turbulent regimes. Eustice [1] was the first to observe the presence of such secondary motions experimentally and also noted that the mass flux decreases with curvature under a fixed pressure gradient. A mathematical proof of the secondary motion's existence was provided by Dean [2,3]. Dean observed that the flow topology can be governed by a single parameter, thereafter called the Dean number:

*dmassaro@kth.se

$\mathrm{De} = \mathrm{Re}_b\sqrt{\delta}$. In this definition, the curvature $\delta = R/R_c$ represents the ratio between the radius of the pipe cross section and the radius of curvature at the pipe centerline, and the bulk Reynolds number $\mathrm{Re}_b = U_b D/\nu$ is based on the bulk velocity $U_b$, the pipe diameter $D$, and the kinematic viscosity $\nu$ of the fluid. The Dean number is interpreted as the ratio of the square root of the product of inertial and centrifugal forces to the viscous forces, representing a measure of the intensity of the secondary flow [4]. The two symmetric, counterrotating vortices have been analytically derived as solutions of the incompressible Navier-Stokes (NS) equations under the small-curvature assumption. Dean's solution is valid for a limited range of flow regimes: $\mathrm{De} < 37.94$ [2] and $\mathrm{De} < 14.14$ [3].

In addition to Dean vortices, there are other noteworthy distinctions between straight and bent pipe flows. Within curved pipes, the flow has a less sudden transition [5] and is significantly more stable, with a critical Reynolds number that can be twice or more as large, see also Refs. [4,6,7]. Sreenivasan and Strykowski [8] conducted experiments on flows in helical pipes, confirming this finding. Up to a certain Reynolds number, they observed that turbulent flow from a straight pipe could relaminarise upon entering a spiral, noting that different transition mechanisms occur at the inner and outer walls. At the inner side, higher harmonics of the perturbation frequency appear as $\mathrm{Re}_b$ is increased, whereas, at the outer wall, transition takes place through the formation and merging of turbulent bursts. Furthermore, the authors found that the flow in the straight section downstream of the helix remains laminar for Reynolds numbers greater than the critical value for undisturbed straight pipes.

Specific to toroidal pipes, Kühnen *et al.* [9,10] conducted experiments to describe the first bifurcation leading to turbulence in a torus, observing a subcritical transition for values of the curvature $\delta \leqslant 0.028$. In agreement with this, the numerical work by Canton *et al.* [11] reported that the flow is unstable to infinitesimal perturbations for all the values of the curvature $\delta$ at least greater than $2 \times 10^{-3}$ because of a Hopf bifurcation, leading to a periodic regime. The existence of two symmetric, counterrotating vortices for any Reynolds number and any nonzero curvature has been analytically and numerically proved by Canton *et al.* [12]. The latter also showed that no flow quantities scale with De when $\delta > 10^{-6}$ and $\mathrm{De} > 10$, and the flow thus requires being studied as a function of two independent parameters: the curvature $\delta$ and the Reynolds number $\mathrm{Re}_b$. The nature of the transition is altered without such a clear separation in the ($\delta$, $\mathrm{Re}_b$) parameter space, which presents a narrow region where two attractors are present. They correspond to two distinct, coexisting transition scenarios, each resulting in different unsteady asymptotic states. In the first scenario, at large curvatures, the flow undergoes a supercritical transition as a consequence of modal instabilities. In the second one, at low curvatures, a subcritical transition to turbulence occurs, triggered by finite-amplitude perturbations [13].

Since toroidal pipe flows represent an idealization of curved pipes, to what extent can the results of the fully developed torus be transferred to limited bends? Does the spatially developing nature of the flow affect the transition mechanism? In the literature, just a few studies attempted to answer these questions. Lupi *et al.* [14] examined the stability properties of flow in a 90°-bend pipe with curvature $\delta = 1/3$ and showed that the flow, steady for $\mathrm{Re}_b \leqslant 2500$, becomes periodic, oscillating with a fundamental Strouhal number $\mathrm{St} = fD/U_b \approx 0.23$ for $\mathrm{Re}_b > 2500$. The global stability analysis highlights a Hopf bifurcation as the cause of the transition from the steady to the periodic regime at $\mathrm{Re}_b = 2531$. Furthermore, the structural sensitivity of the unstable eigenmode to spatially localized feedback reveals that the region located 15° downstream of the bend inlet on the outer wall is the most receptive to such perturbations, suggesting that the instability is linked to the strong shear by the backflow phenomena in the outer-wall separation bubble. We thus aim to perform a similar analysis for the 180°-bend pipe with a unique numerical approach. The adaptive mesh refinement (AMR) technique is used to obtain independent meshes for each solution field, e.g., the base flow and the perturbation, both designed to minimize the committed error. Along with the numerical methodology, this paper consists of the description of the transition mechanism for such curved geometry. To our knowledge, the only study on transition in the 180°-bend pipe is that by Hashemi

*et al.* [15]. However, they do not address the nature and cause of transition, as no actual stability calculation is performed. They also estimate an exceptionally high critical Reynolds number.

The remainder of the paper is organized as follows: First, we introduce the numerical methodology, including information about the AMR application for stability studies. Next, we discuss the global stability analysis in Sec. IV, which involves the examination of the base flow and the determination of both the direct and adjoint unstable eigenmodes. Then, Sec. V explores the instability's nature through the structural sensitivity map. Finally, we conclude with our findings and prospects in Sec. VI.

## II. NUMERICAL FRAMEWORK

In the current paper, we compute the numerical solution of the incompressible NS equations, along with the linearized direct and adjoint (dual) solutions. We prescribe a Dirichlet condition with a parabolic (Hagen-Poiseuille) velocity profile at the inlet, and the outflow consists of natural boundary condition $(-p\mathcal{I} + \nu\boldsymbol{\nabla u}) \cdot \mathbf{n} = 0$, where $\mathbf{n}$ is the normal vector. In the linear simulations, we set a sponge layer at the outflow, with a length of $1D$, and a forcing function adapted from Nordström *et al.* [16], to avoid reflections from the boundary. The pipe surface is a no-slip and impermeable wall. Different initial conditions are used for the linear and nonlinear simulations, as specified below. The simulations are carried out using the open-source code Nek5000 [17], based on a spectral-element method [18]. This formulation offers minimal dissipation and dispersion, with high accuracy and almost exponential convergence. Similarly to a high-order finite element method, the computational domain is divided into nonoverlapping hexahedral subdomains called elements. Each element is considered a spectral domain where the velocity and pressure solutions are based on the Lagrangian interpolants defined on the Gauss-Lobatto-Legendre (GLL) or Gauss-Legendre (GL) points, respectively. The $\mathbb{P}_N - \mathbb{P}_{N-2}$ formulation employs $p+1$ GLL points for velocity and $p-1$ GL points for pressure. In our simulations, the polynomial order $p$ is set to 7 after a proper convergence study. The time integration is performed via third-order implicit backward differentiation, with an extrapolation scheme of order three for the convective term. In addition, the advection term is also overintegrated, or dealiased, to retain its skew-symmetry [19].

Similarly to Lupi *et al.* [14], the computational domain consists of two straight sections, connected by a 180°-bend with a curvature radius equal to three times the radius of the pipe, i.e., $\delta = R/R_c = 1/3$. During the simulations, the NS equations are expressed in the Cartesian reference frame. However, in the postprocessing stage, a local reference system $(s, p, y')$ is introduced. The direction of the coordinate $y'$ is unchanged compared to $y$, $s$ is the streamwise coordinate along the pipe centerline with the origin at the bend exit, and $p$ is given by the right-hand triad with $y'$ and $s$. This reference system can be seen as a Frenét frame with the $p$ unit vector inverted and with the angle $\theta$ measuring the location in the bend, starting from $z = 0$ (positive $x$-axis) and clockwise (see Fig. 1). We refer to the $xy$ and $xz$ planes as the symmetry and cross planes, respectively. The initial nonlinear simulation and the base flow computation are performed on a mesh with straight inflow and outflow pipe sections which are $10D$ and $20D$ long, respectively. For the direct and dual solution, we consider a smaller pipe with a $6D$ inflow (outflow) length. The mesh is made symmetric (same inflow and outflow length) for the structural sensitivity analysis, with an outflow reduction for truncating the convective growth of the instability. Nonetheless, following Lupi *et al.* [14], the influence of the computational domain size is carefully assessed.

### A. Mesh adaptivity

The current paper aims to use the AMR technique to obtain independent meshes designed for the nonlinear base flow, direct, and dual linear solutions. In this section, first we introduce the used computational tools and then we describe the general workflow for the meshing procedure.

The numerical framework has been developed by our group in the spectral-element code Nek5000 [20–23]. The AMR has been recognized as a crucial advancement in numerical

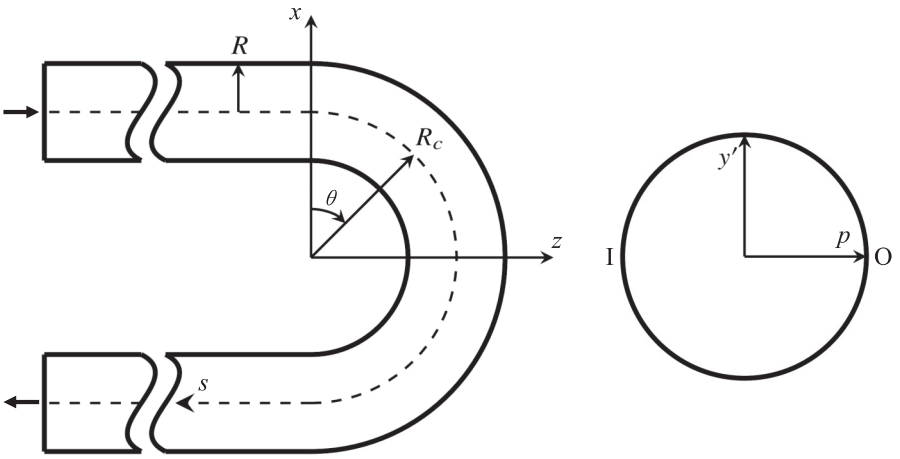


FIG. 1. Sketch of the 180°-bend pipe geometry with black arrows indicating the inflow and outflow directions. The reference systems are reported in the (left) symmetry and (right) cross planes.

simulations by Slotnick *et al.* [24]. This is due to its ability to provide greater flexibility in meshing, allowing for adjustments to be made on the fly based on real-time or time-averaged estimations of computational errors. Our previous usage of AMR focused on direct numerical simulations (DNSs) of incompressible turbulent flows, see Refs. [25,26]. However, the application of AMR in three-dimensional global stability analysis required the adaptation of the code to the linear solver and other stability tools as well. For the interested reader, further details are provided in an exploratory work that was conducted to validate the framework in a two-dimensional setting [27]. In the investigation of transitional flows, the appropriate mesh resolution is pivotal, probably even more than in fully turbulent flows. This is because an under-resolved mesh can lead to the identification of incorrect underlying physical mechanisms. Therefore, we utilize AMR to obtain multiple independent meshes that are optimized for the specific solution field being investigated.

Accurate measurement of the error is a prerequisite for designing an adequate mesh. In this case, we employ the spectral error indicator (SEI), which was initially proposed by Mavriplis [28]. The SEI assesses both the truncation and quadrature errors that occur in the solution field, which depends on the nature of the problem at hand. For instance, in the case of nonlinear DNS, performed for extracting the base flow, the velocity field is considered, whereas for linear DNS, the direct and dual perturbation velocity field is assessed for the direct and adjoint problems, respectively. Regardless of the solution field, the error indicator $\epsilon$ is estimated as follows. For the sake of simplicity, we consider a $1D$ problem, where $u$ is the exact solution to a system of partial differential equations and $u_N$ is an approximate spectral-element solution with polynomial order $N$. We expand $u(x)$ on a reference element in terms of the Legendre polynomials,

$$u(x) = \sum_{k=0}^{\infty} \hat{u}_k L_k(x), \tag{1}$$

where $\hat{u}_k$ are the associated spectral coefficients and $L_k(x)$ is the Legendre polynomial of order $k$. The estimated error $\epsilon = \|u - u_N\|_{L^2}$ results in

$$\epsilon = \left( \int_N^{\infty} \frac{\hat{u}(k)^2}{\frac{2k+1}{2}} dk + \frac{\hat{u}_N^2}{\frac{2N+1}{2}} \right)^{\frac{1}{2}}. \tag{2}$$

Assuming a decay of the spectral coefficients of the form $\hat{u}(k) \approx c \exp(-\hat{\sigma} k)$, the parameters $c$ and $\hat{\sigma}$ are obtained by least-squares fitting of the (usually four) base functions $u_k$ with the highest

frequencies. This operation is performed for each dimension separately. In the actual 3D case, the maximum error among each component is considered. The error is measured online and $\epsilon$ indicates the error per element at each time step. Eventually, the time average of $\epsilon$ for a given interval $T$ is considered. The elements with the largest SEI are isotropically split to increase the spectral resolution (isotropic $h$-type refinement). The single parent element is replaced with eight children in three-dimensional cases [29]. Following Kruse [30], we use the conforming-space and nonconforming-mesh approach, in which the hanging nodes are not considered as real degrees of freedom and nonconforming interfaces are treated with an interpolation operator. Massaro *et al.* [23] showed the nonconforming interfaces do not affect the solution field or introduce any further instabilities. Peplinski *et al.* [31] measured that the excellent parallel performance of Nek5000 [32] are not affected by the AMR implementation.

Regarding the meshing procedure, further details are needed to clarify the workflow. Starting from the nonlinear DNS, the base flow is extracted. After the transient, required by the initial condition to adapt, several rounds of refinement are performed to enhance the mesh quality. Since the refinement strategy remains consistent for both nonlinear and linear simulations, the approach is explained once and for all for the direct problem, in a few lines below. In the nonlinear simulations, we use a domain larger than Lupi *et al.* [14] and Hashemi *et al.* [15]: $10D$ and $20D$ for the inflow and outflow lengths, respectively. The base flow, extracted using SFD, is then spectrally interpolated on a mesh which is reduced for truncating the convective growth of the instability, and symmetric (with straight sections of the same lengths) for performing the structural sensitivity analysis. The interpolation is also required to start the linear simulation on a fresh spectral grid. Particularly, we perform a spectral interpolation, with an accuracy that corresponds to the adopted polynomial order ($p = 7$) [33]. The effects of the mesh reduction and the base flow interpolation have been carefully assessed to make sure the instability mechanism is not altered by them. Subsequently, the linear DNS of the direct and dual linear problem is carried out by initializing the perturbation field with spatially uncorrelated noise. After the initial transient, which can be determined by looking at local (velocity probes) and global (total perturbation energy) quantities, the velocity perturbation field is used to improve the mesh quality by performing $h$ refinement. The SEI is computed on the current solution field, averaged for a reasonable time interval, and used as a measure of the truncation and quadrature error [28]. Therefore, the resolution is automatically improved in the regions indicated by the SEI. Multiple rounds of refinement are conducted and, at each round, the total amount of elements is increased by a user-defined percentage. Specifically, in our case, the elements where the SEI is the largest are refined to increase the overall number of elements by 15%. This criterion is particularly suitable for static memory allocation codes like Nek5000. A standard mesh convergence analysis is performed to terminate the process. A similar procedure is followed for the linear dual solutions. Ultimately, three independent meshes are generated for the base flow, linear direct, and dual solutions, respectively, each designed to reduce numerical errors. Especially, the direct and dual solutions necessitate considerably different meshes. Indeed, the non-normality of the NS operator leads to a significant spatial separation between them, as depicted in Fig. 2. Note that the wavemaker evaluation, necessary for the structural sensitivity analysis discussed in Sec. V, requires the direct and dual solution defined onto the same mesh. Thus, in this last postprocessing step, the linear solutions are spectrally interpolated and the structural sensitivity is computed. The outcomes have shown to be robust with respect to the chosen interpolating mesh in this last step.

There are critical aspects that will require attention in the future. One of the pressing questions is the definition of a criterion for terminating the refinement process. Unlike turbulent flows, where statistical approaches can be employed [26,34], global stability analysis lacks a clear criterion. In the present paper, standard mesh convergence analysis is utilized, which involves examining the convergence of local and global quantities. Another potential future direction may involve employing multiple meshes for each of the $m$ eigenvalues during the Arnoldi calculation. However, implementing multiple meshes during the same simulation is currently unavailable in the spectral-element code Nek5000. Note that typically the most unstable (most dangerous) mode is sought. Despite the aforementioned limitations, this application of AMR in the study of transitional flows,

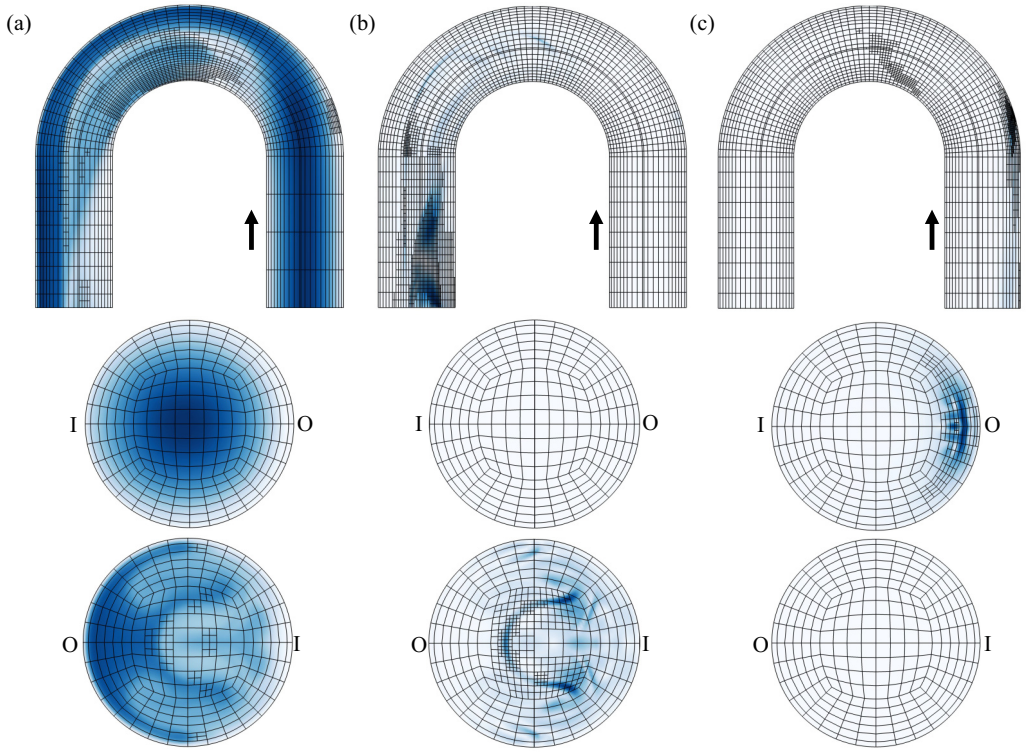


FIG. 2. Spectral-element grid for different meshes designed via AMR technique for the (a) nonlinear base flow, the linear (b) direct, and (c) dual solutions, respectively. From top to bottom: The symmetry plane ($y = 0$) and the cross planes at the inlet ($\theta = 0$) and outlet ($\theta = 180^\circ$) of the bend. Blue isocontours of the velocity magnitude normalized between $[0, U_b]$ for the base flow and [0,1] (i.e., the maximum) for the linear and dual solutions. In the symmetry plane view, a shortened domain is shown with inflow and outflow lengths equal to $2D$. The black arrows indicate the base flow direction.

using different and independent meshes (adapted to the specific solution), provides interesting and encouraging results. The main advantage consists of the capability of the code to automatically adapt the mesh to the unstable eigenmode, minimizing the source of numerical errors. Once the meshes are converged, they are employed in solving the nonlinear and linearized NS equations, as well as for computing the spectrum of eigenvalues using the Arnoldi method.

## III. NONLINEAR BASE FLOW

The literature lacks stability analysis of the 180°-bend pipe flow. Only Hashemi *et al.* [15] presents DNS of such transitional flow for the curvature $\delta = R/R_c = 1/3$. Hence, we first compute the numerical solution of the incompressible NS equations, which in the nondimensional form read

$$\frac{\partial \boldsymbol{u}}{\partial t} + (\boldsymbol{u}\cdot\boldsymbol{\nabla})\boldsymbol{u} = -\boldsymbol{\nabla} p + \frac{1}{\mathrm{Re}_b}\nabla^2\boldsymbol{u},$$
$$\boldsymbol{\nabla}\cdot\boldsymbol{u} = 0, \tag{3}$$

where $\boldsymbol{u}$ is the velocity vector, $p$ is the nondimensional pressure, and $\mathrm{Re}_b = U_b D/\nu$ is the Reynolds number based on the pipe diameter $D$, the bulk velocity $U_b$, and the kinematic viscosity $\nu$. To complete the set of equations, proper initial and boundary conditions are considered.

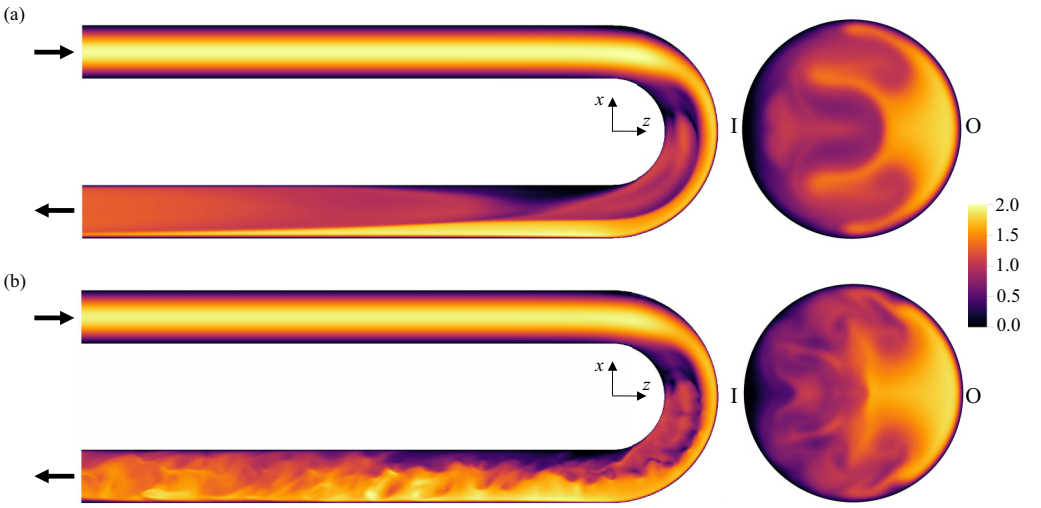


FIG. 3. Velocity magnitude field computed via nonlinear DNS after 200 convective time units ($D/U_b$) at (a) $\mathrm{Re}_b = 2500$ and (b) $\mathrm{Re}_b = 3000$. The $xz$ symmetry plane and the $xy$ cross plane at $z = 0$ (bend outlet) on the left and right, respectively. The black arrows indicate the inflow and outflow directions. The inner and outer walls are marked with letters I and O

Hashemi *et al.* [15] showed that the critical Reynolds number is $\mathrm{Re}_b = 5000 - 5200$, based on the bulk velocity, kinematic viscosity, and pipe diameter. As expected, the critical $\mathrm{Re}_{b,\mathrm{cr}}$ is much higher than the straight pipe case. However, their estimation is far greater than the transitional Reynolds number reported by previous studies for the same curvature $\delta = 1/3$, particularly $\mathrm{Re}_{b,\mathrm{cr}} = 2531$ [14] and $\mathrm{Re}_{b,\mathrm{cr}} = 3290$ [11], for the 90°-bend and toroidal pipes with the same curvature, respectively. We thus would expect a critical Reynolds number falling within this range for a case that is intermediate to the aforementioned ones. Indeed, our DNS of the nonlinear NS equations shows clearly that the first instability occurs for $\mathrm{Re}_b = 2500 - 2600$. Already at $\mathrm{Re}_b = 3000$, the flow is fully turbulent; see Fig. 3. It is unlikely to be a coincidence that our estimation precisely halves the value reported by Hashemi *et al.* [15], who may have an inconsistency in reporting the value of $\mathrm{Re}_b$ by using the centerline velocity instead of the bulk velocity as reference. This is also evident from Fig. 12 by Hashemi *et al.* [15], where the color scale ranges from 0 to 1.

With this in mind, we can proceed to obtain the base flow for a Reynolds number $\mathrm{Re}_b = 2550$ slightly higher than the largest value of $\mathrm{Re}_b$ where the flow remains steady ($\mathrm{Re}_b = 2500$). At $\mathrm{Re}_b = 2550$, the nonlinear DNS confirms that both the 90°- and 180°-bend pipe flows exhibit a time-periodic behavior with a period $T \approx 4.3$ convective time units ($D/U_b$). Local probe measurements are also used to identify the appearance of a limit cycle in the phase space representation, see Fig. 4(b). At this Reynolds number, the lowest for which the flow exhibits an unsteady behavior among the considered values, the separation bubbles (see Fig. 4) oscillate with a Strouhal number $\mathrm{St} = fD/U_b = 0.23$, where $f$ is the frequency. The results of the nonlinear simulations are in excellent agreement with the stability analysis outcomes, which report a globally unstable eigenmode characterized by a similar frequency ($\mathrm{St} = 0.233$), as discussed in Sec. IV. The consistent patterns observed in both 90°- and 180°-bend pipe flows lead us to hypothesise that a common underlying physical mechanism is responsible for triggering the transition in both cases. Note that we did not observe any hysteresis when going from laminar to turbulent, as opposed to Hashemi *et al.* [15].

### A. Base flow

As the stability analysis deals with the study of the evolution of infinitesimal perturbations to a base state, we first need to calculate the base flow about which the NS equations are linearized. In

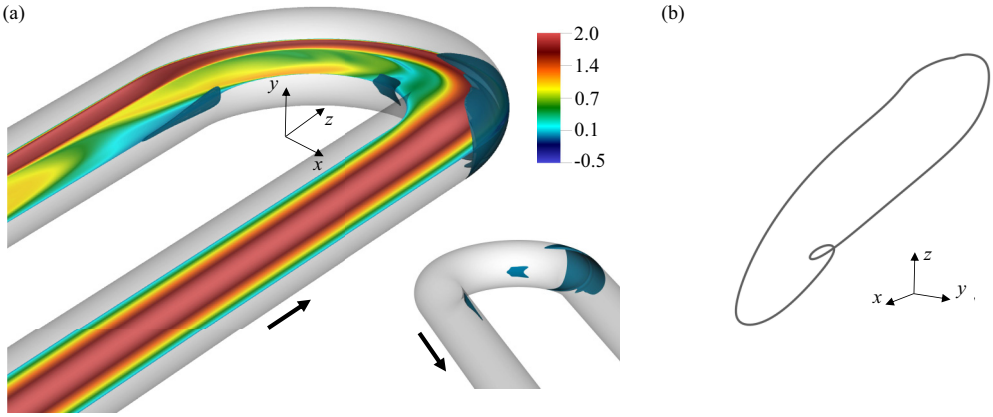


FIG. 4. (a) Isocontours of the streamwise velocity $u_s$ in the symmetry plane ($y = 0$) for the base flow extracted via SFD at $\mathrm{Re}_b = 2550$. The blue three-dimensional isosurface for $u_s \leqslant 0$ shows the three distinct recirculation regions, symmetric with respect to the $xz$ plane. The black arrows indicate the flow direction. (b) Phase-space representation of local velocity measurements of a probe located at ($x = -1.30D$, $y = -0.35D$, $z = -4.00D$) for the nonlinear DNS of the 180°-bend pipe flow at $\mathrm{Re}_b = 2550$.

the current paper, the steady base flow $(\boldsymbol{U}, P)$ at $\mathrm{Re}_b = 2550$ is extracted via selective frequency damping (SFD) [35] from nonlinear NS equations. The SFD technique damps the oscillations of the solution using a temporal low-pass filter. It applies to the flow a forcing $\boldsymbol{f}$ defined as $\boldsymbol{f} = -\chi(\boldsymbol{u} - \boldsymbol{w})$, where $\boldsymbol{u}$ is the velocity solution and $\boldsymbol{w}$ is the temporally low-pass filtered velocity obtained by a differential exponential filter $\boldsymbol{w}_t = (\boldsymbol{u} - \boldsymbol{w})/\Delta$, with $\Delta$ determining the filter width. To assess the convergence, we consider the amplitude of the forcing $\varepsilon = \|\boldsymbol{u} - \boldsymbol{w}\|_{L^2(\Omega)}$. The tolerance level of $\varepsilon \approx 10^{-7}$ is achieved. For the base flow, as for the direct and dual solutions, the mesh is designed via the AMR technique.

Figure 5 displays the base flow extracted using SFD at $\mathrm{Re}_b = 2550$, which resembles the steady flow at $\mathrm{Re}_b = 2500$. Additionally, we compare it with the base state computed by Lupi *et al.* [14] for the 90°-bend pipe, at the same $\mathrm{Re}_b = 2550$ and curvature $\delta = 1/3$. In both, the parabolic velocity profile starts to deviate slightly just upstream of the bend inlet. Figure 5(a) shows the evolution of the flow in the bend at the angles $\theta = 0°$, 45°, 75°, 90°, 120° and 180° (panels *A, B, C, D, E,* and *F*). Both flows exhibit a similar structure within the 0°–90° range. In the panel labeled *D*, which constitutes the outlet and midpoint of the bend for the 90° and 180° pipes, respectively, Dean vortices are visible in the center of the pipe. Additionally, two smaller ones are located close to the inner wall. The discrepancy with the torus, where only one pair of vortices shows up, is evident [12].

Furthermore, unlike a toroidal geometry where no separation occurs, both spatially developing bent pipes exhibit at least two separation bubbles. One is situated on the outer wall of the pipe, beginning at $\theta \approx 0°$ (actually, a few degrees before the inlet) and reattaching at $\theta = 30°$, while the other is located on the inner side, approximately 67.5° downstream of the bend inlet, see Fig. 4(a). The reader can also refer to Fig. 4 in Lupi *et al.* [14] for the 90° case. The backflow region on the outer wall at the bend inlet displays the most negative value, with the maximum absolute value of the streamwise velocity equal to almost 50% of the bulk velocity. In addition, the 180° case presents a third recirculation bubble. It extends from the bend outlet up to $s = 2D$ on the inner wall, with a maximum backflow velocity around 2% of the bulk velocity. All the recirculation regions exhibit a symmetry with respect to to the $xz$ plane.

As the curved section in the 180°-bend pipe flow is twice as long as in the 90° case, the centrifugal force acting on the flow persists for twice the length. Consequently, at the end of the bend, the outflow becomes highly concentrated towards the outer side and the central areas. It resembles a horizontal (IO plane) symmetric shape rather than being more uniformly distributed only along the

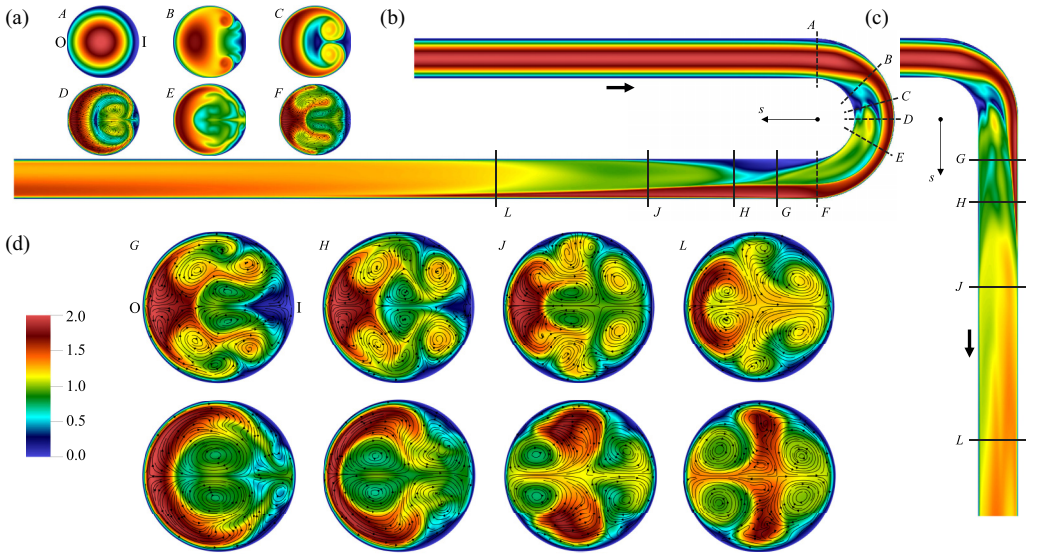


FIG. 5. Planar perspectives of the base flow extracted via SFD at the Reynolds number $\mathrm{Re}_b = 2550$ (curvature $\delta = 1/3$). (a) The variation of velocity magnitude in circular cross sections of the bend is illustrated at various angles, including $\theta = 0°$, 45°, 75°, 90°, 120°, and 180° (*A, B, C, D, E,* and *F,* respectively). In addition, the in-plane streamlines are shown at 90° (panel *D*) and 180° (panel *F*). (b), (c) Isocontours of velocity magnitude in the *xz* plane at $y = 0$ for the 180° and 90° bent pipes, respectively. (d) Lastly, the velocity magnitude and in-plane streamlines for the 180°-bend (in the first row) and 90°-bend (in the second row) are shown for *G, H, J,* and *L*, respectively, at various streamwise stations $s = 1D$, $s = 2D$, $s = 4D$, and $s = 8D$.

wall [Fig. 5(a), panels *D* and *F*]. Lupi *et al.* [14] described the pattern of four Dean vortices formed at the bend outlet, with two large structures near the center of the pipe cross section and two small ones located close to the inner wall [Fig. 5(a), panel *D*]. The outlet of the current case is significantly different: a system of eight Dean vortices, is formed. As the configuration is nearly symmetric with respect to the horizontal midaxis, just the lower part is described below. A large structure appears near the center, close to two smaller and corotating (and counterrotating with respect to to the central one) vortices. Furthermore, a vortical structure appears at the bottom of the cross section, pushed towards the wall by the central vortices.

Looking at the outflow, Fig. 5(d) presents a comparison of the base flow at various distances from the bend outlet, specifically $s = 1D$, $s = 2D$, $s = 4D$, and $s = 8D$, for the 90°- and 180°-bend pipe flows (in the first and second rows, respectively). In-plane streamlines are used for the characterization of the base flow and the identification of Dean vortices. Following the spatial evolution downstream of the bend, the two corotating structures and the bottom Dean vortex get larger at $s = 1D$. In addition, at the outer wall, where an intense shear layer develops, one more vortex appears. At this stage, the formation counts ten Dean vortices overall (panel *G*). At $s = 2D$ (panel *H*), the pattern is shrunk downstream of the recirculation region described above, which is a characteristic of the 180° case only. Further downstream ($s = 4D$), one sees an incipient merging of the left-side vortex with the central one and the expansion of one of the two corotating vortices (section *J*). The lower structure is now confined in the bottom right corner. Eventually, at $s = 8D$, four out of five initial vortices are merged into two larger swirls. The bottom structure still persists (panel *L*). Overall, the six Dean vortices state is weakly asymmetric, with a magnitude which grows with the distance downstream of the bend, but without substantial differences between the two halves of the pipe cross section. In summary, the overall pattern of the base flow is different from

the four Dean vortices state described by Lupi *et al.* [14] for the 90°-bend pipe flow and departs from the fully developed toroidal flow, where only one pair of Dean vortices is detected [12].

## IV. GLOBAL STABILITY ANALYSIS

In the current section, the results of the global stability analysis are presented. The base flow previously extracted via SFD is used to linearize the NS equations. The linear direct and adjoint eigenmodes, along with their associated eigenvalues, are computed. The most unstable eigenmode is presented and compared to the 90°-bend pipe flow results [14].

### A. Linear direct numerical simulations

To investigate the unstable eigenmode, we start by performing a set of linear simulations. The NS equations are linearized about the extracted base flow, deriving the governing equations for the perturbations $(\boldsymbol{u}', p')$,

$$\frac{\partial \boldsymbol{u}'}{\partial t} + (\boldsymbol{u}'\cdot\nabla)\,\boldsymbol{U} + (\boldsymbol{U}\cdot\nabla)\,\boldsymbol{u}' = -\nabla p' + \frac{1}{\mathrm{Re}_b}\nabla^2\boldsymbol{u}',$$
$$\nabla\cdot\boldsymbol{u}' = 0, \tag{4}$$

completed by proper initial and boundary conditions. The simulations are initialized with noise uncorrelated in space, which has a nonzero projection on the wanted modes, and a frozen base flow (previously extracted via SFD). We expect the perturbation solution to converge to the most unstable eigenmode of the direct problem Eq. (4) [36].

Similarly, we compute the dual solution $(\boldsymbol{u}^\dagger, p^\dagger)$ for the linearized adjoint set of equations

$$-\frac{\partial \boldsymbol{u}^\dagger}{\partial t} - (\boldsymbol{U}\cdot\nabla)\,\boldsymbol{u}^\dagger + (\nabla\boldsymbol{U})^T\boldsymbol{u}^\dagger = \nabla p^\dagger + \frac{1}{\mathrm{Re}_b}\nabla^2\boldsymbol{u}^\dagger,$$
$$-\nabla\cdot\boldsymbol{u}^\dagger = 0, \tag{5}$$

supplemented by proper initial and boundary conditions. Similarly to the direct problem, the dual perturbation from Eq. (5) converges to the most unstable adjoint eigenmode.

The simulations are initialised with a mesh which is gradually refined according to the procedure described in Sec. II. As a result, we obtain independent meshes for the direct and dual solutions, which are designed by minimizing the committed numerical error. Both the direct and the adjoint simulations are run for a sufficiently long time interval after the last AMR refinement, approximately 100 convective units $(D/U_b)$. The converged perturbation solutions, $\boldsymbol{u}'$ and $\boldsymbol{u}^\dagger$, are shown in Fig. 6. As expected, they resemble the real part of the unstable eigenmode computed via the Arnoldi method, see the discussion in Sec. IV B. The comparison with the 90°-bend (same $\mathrm{Re}_b$ and $\delta$) shows in a clear way that very similar perturbations are obtained, which then trigger the transition (Fig. 6). The structure has a ring shape near the separation bubble on the outer wall of the pipe and moves towards the inner wall as the distance increases along the bend. Eventually, it evolves into a larger structure downstream of the bend. Interestingly, the origin of the $xz$-symmetric structure corresponds to the recirculation area pointed out in Fig. 4. Similarly, the dual solution corresponds to the real part of the unstable adjoint mode and the shape resembles the 90°-bend flow solution.

Overall, the two perturbation solutions, $\boldsymbol{u}'$ and $\boldsymbol{u}^\dagger$, evolve in distinct regions of the domain (Fig. 6). The AMR application allows having different independent meshes which are optimized for the solution field under investigation. The resulting meshes are also used for the spectrum calculation discussed in the following section.

### B. Spectrum of the eigenvalues

The growth rate $(\sigma)$ and angular frequency $(\omega)$ of the unstable eigenmode can be determined through the exponential power method [37]. One limitation of this approach is its inability to

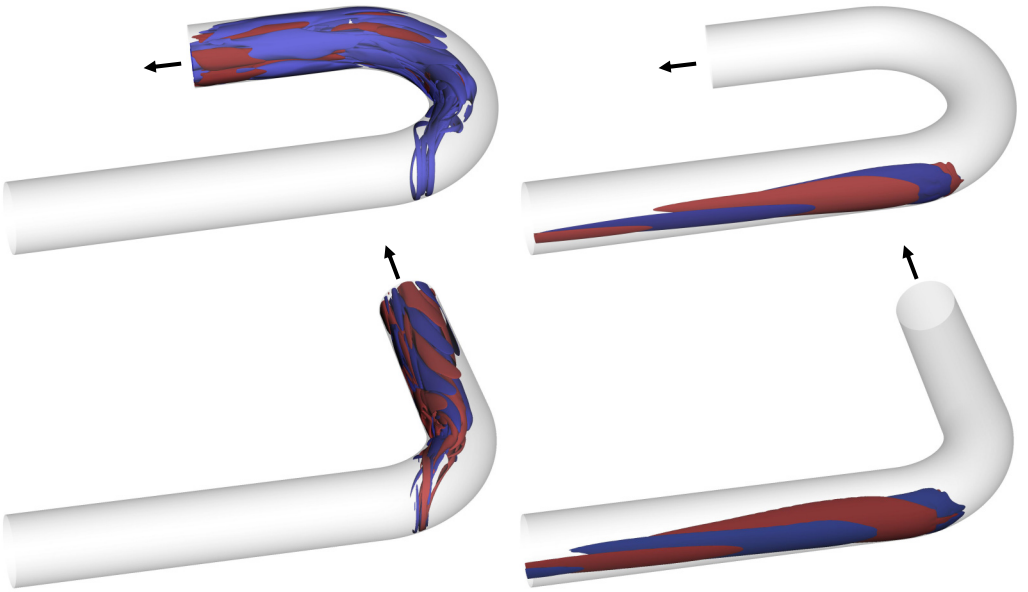

FIG. 6. Isosurfaces of the (blue) negative and (red) positive streamwise velocity component $u_s$ of the perturbation solution for $\mathrm{Re}_b = 2550$ of the (left) direct and (right) dual problem. The values are in the range $[-0.1, 0.1]$ of the maximum for the (top) 180°- and (bottom) 90°-bend pipes. For the sake of clarity, a shortened domain is shown with inflow and outflow lengths equal to $5D$ and $3D$, respectively. The black arrows indicate the flow direction. Note that the phases of the disturbances are arbitrary and thus not directly comparable between the two cases.

evaluate the full spectrum of eigenvalues. Indeed, it is not possible to determine if there is only one unstable eigenvalue or multiple ones.

To address this limitation, we compute a portion of the spectrum of eigenvalues for both the direct and adjoint linearized NS operators. The velocity and pressure disturbance of the linear problem Eq. (4) can be expressed as

$$\begin{aligned} \boldsymbol{u}'(\mathbf{x}, t) &= \hat{\boldsymbol{u}}(\mathbf{x}) e^{\lambda t}, \quad \lambda \in \mathbb{C}, \\ p'(\mathbf{x}, t) &= \hat{p}(\mathbf{x}) e^{\lambda t}, \quad \lambda \in \mathbb{C}, \end{aligned} \tag{6}$$

under the normal-mode hypothesis, with $\lambda = \sigma + i\omega$. The same approach is applied to the problem Eq. (5). Afterwards, the generalized eigenvalue problem is formulated by substituting Eqs. (6) in Eq. (4):

$$\lambda \mathcal{R} \hat{\mathbf{r}} = \mathcal{J} \hat{\mathbf{r}}, \tag{7}$$

where

$$\hat{\mathbf{r}} = \begin{pmatrix} \hat{\boldsymbol{u}} \\ \hat{p} \end{pmatrix}, \quad \mathcal{R} = \begin{pmatrix} \mathcal{I} & 0 \\ 0 & 0 \end{pmatrix}, \quad \mathcal{J} = \begin{pmatrix} -\nabla \boldsymbol{U} - \boldsymbol{U} \cdot \nabla + \dfrac{1}{\mathrm{Re}_b} \nabla^2 & -\nabla \\ \nabla \cdot & 0 \end{pmatrix}. \tag{8}$$

The explicit solution of the problem Eq. (7) requires large memory storage and prohibitive computational cost. Alternatively, it can be reformulated as an initial value problem for the velocity only by exploiting the incompressibility constraint, i.e., eliminating the pressure [38]. The solution has the form

$$\boldsymbol{u}(\mathbf{x}, t) = e^{\mathcal{L} t} \boldsymbol{u}_0(\mathbf{x}), \tag{9}$$

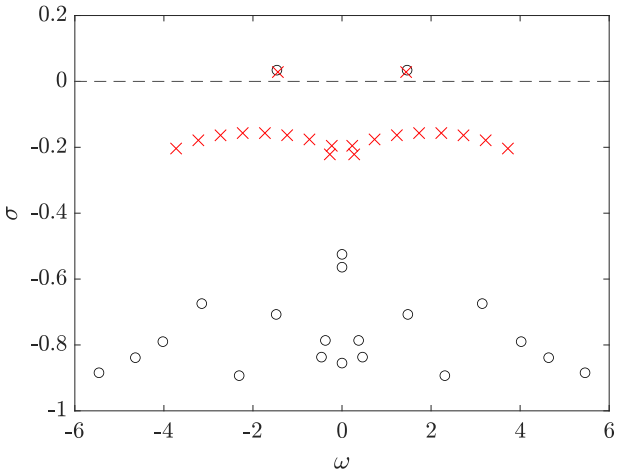


FIG. 7. Portion of the spectrum for the direct problem at $\mathrm{Re}_b = 2550$ of the (cross) 90° and (circle) 180° bent pipe flows.

where $\mathcal{L}$ is the projection of $\mathcal{J}$ on a divergence-free space and $k$ are the eigenvalues of the matrix exponential $e^{\mathcal{L}t}$, related to those of $\mathcal{J}$ by the expressions

$$\sigma = \frac{\ln(|k|)}{\Delta t}, \quad \omega = \frac{\arg(k)}{\Delta t}, \tag{10}$$

with $\Delta t$ being the time interval between the Krylov vectors generated in the time-stepper approach, as described by Bagheri *et al.* [39]. The eigenpairs are computed with the implicitly restarted Arnoldi method, proposed by Sorensen [40] and implemented in the software package ARPACK [41]; see also Refs. [39,42,43]. In the Arnoldi method, the eigenpairs are approximated by seeking solutions in the Krylov subspace of dimension $m = 100$. The first 20 eigenpairs for both the direct and adjoint problems are calculated and the residual tolerance is set to $10^{-6}$ for the eigenvalue computation. In addition, the Ritz estimate for all eigenvalues is at least two orders of magnitude smaller than this tolerance.

The spectrum confirms a single unstable eigenmode with the growth rate $\sigma = 0.0342$ and angular frequency $\omega = 1.462$, see Fig. 7. The same calculation is performed for the adjoint linearized NS operator, whose eigenvalues correspond to the spectrum of the direct (the maximum relative difference between the growth rates of the direct and adjoint eigenvalues is below $10^{-3}$). The shape of the direct and dual unstable eigenmode corresponds, as expected, to the solutions obtained via a linear response (Fig. 6). As the unstable mode is associated with a couple of complex conjugate eigenvalues, the spectrum analysis confirms that the flow undergoes a Hopf bifurcation between $\mathrm{Re}_b = 2500$ and $\mathrm{Re}_b = 2550$. A more accurate estimate of the critical Reynolds number is obtained by linearly interpolating the growth-rate values of the least stable mode at $\mathrm{Re}_b = 2500$ and $\mathrm{Re}_b = 2550$. For the 180°-bend flow, the critical Reynolds number is estimated to be $\mathrm{Re}_{b,\mathrm{cr}} \approx 2528$, very close to the 90°-bend pipe ($\mathrm{Re}_{b,\mathrm{cr}} = 2531$, see Ref. [14]), and significantly lower than the value computed for a toroidal pipe with the same curvature ($\mathrm{Re}_{b,\mathrm{cr}} = 3290$, see Ref. [11]).

The linear stability analysis is further validated by data from nonlinear DNSs. The nonlinear simulations are initialized with a Poiseuille profile with superimposed a divergence-free spatially uncorrelated noise. Discarding the initial transient, each simulation is time integrated for approximately 400 convective time units. From local velocity probes, the amplitude of the perturbations can be estimated. The saturation amplitude (normalized by the value at $\mathrm{Re}_b = 2800$) is shown in Fig. 8. For a supercritical Hopf bifurcation, the size of the limit cycle is supposed to grow continuously from zero and increases proportionally to $\sqrt{\mathrm{Re}_b - \mathrm{Re}_{b,\mathrm{cr}}}$ [36]. The data exhibits an

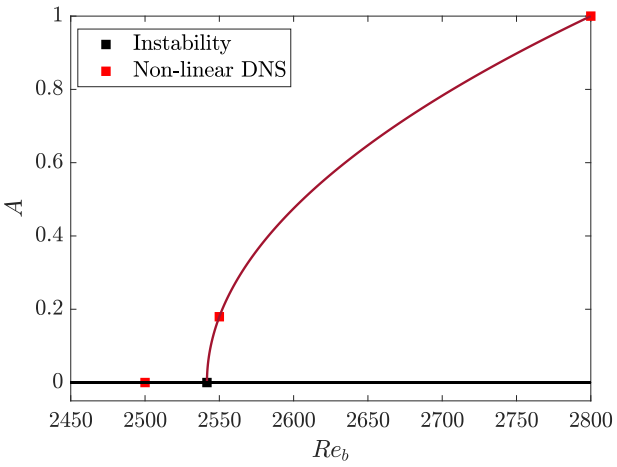


FIG. 8. The growth of the amplitude of the limit cycle. From local velocity probes, the saturation amplitude, $A$, measured as a function of Reynolds number (red line). The nonlinear DNS data (red squares) fit the function $A \sim \sqrt{\mathrm{Re}_b - \mathrm{Re}_{b,cr}}$. The intercept (black square) of the red line with the horizontal axis (black line) provides a critical Reynolds number approximately equal to 2538.

excellent fit to the function $A = C\sqrt{\mathrm{Re}_b - \mathrm{Re}_{b,\mathrm{cr}}}$ that describes the growth of the amplitude of the limit cycle. The intercept of the curve with the horizontal axis provides a critical Reynolds number approximately equal to 2538, which is very close to the value estimated from the results of the global stability analysis. The critical Reynolds number found in the current paper is approximately half the prediction made by Hashemi *et al.* [15]. As previously suggested, this difference may be due to an inconsistent normalization of the velocity field by Hashemi *et al.* [15], who used the centerline velocity instead of the declared bulk velocity. Furthermore, Hashemi *et al.* [15] reported sensitivity to the amplitude of the initial disturbance for $5000 < \mathrm{Re}_b < 5200$, which is an indicator of subcritical transition. Nevertheless, such a scenario is not observed in the present work.

## V. STRUCTURAL SENSITIVITY ANALYSIS

The adjoint of a linear operator is a crucial concept of functional analysis, as it allows, among other things, the identification of regions with the highest receptivity to initial conditions. In the case of 180°-bend pipe flow, the regions of maximum receptivity are concentrated in the outer part of the inflow and at the beginning of the bending section, as depicted in figure 6. Overall, the receptivity decays rapidly in the pipe cross-plane. Inside the curve, it does extend up to $\theta = 21°$. However, analyzing the adjoint (and direct) mode independently does not provide conclusive information about the origin of the instability. Thus, we conduct a structural sensitivity analysis.

According to Chomaz [44], the flow advection term $-(\boldsymbol{U}\cdot\boldsymbol{\nabla})\,\boldsymbol{u}^\dagger$ is the primary cause of the non-normality of the linear operator, resulting in upstream transport for the adjoint perturbations. This non-normality, in turn, leads to the substantial spatial separation between the direct and adjoint eigenmodes [44–46]. Due to this significant separation between the two, alternative methods are necessary to pinpoint the origin of the instability. Similarly to Chomaz *et al.* [47] and Monkewitz *et al.* [48], the work by Giannetti and Luchini [49] introduces the idea of a wavemaker for global modes. By applying this concept, it becomes possible to examine the spatial location where a modification in the problem structure results in the largest shift of the eigenvalue. This drift indicates that the structural perturbation affects the core of the instability mechanism.

Therefore, we proceed to examine the spatial distribution of the structural sensitivity function $\eta$, which identifies the locations where the feedback is stronger, i.e., the regions where the instability

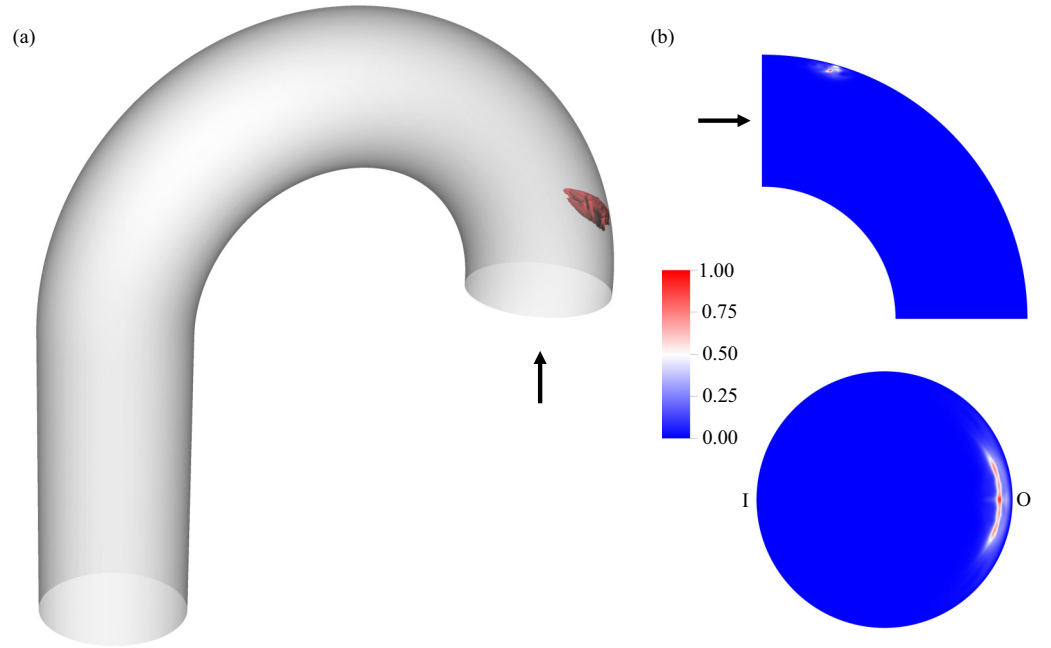


FIG. 9. Structural sensitivity map of the 180°-bend pipe flow normalized between 0 and 1. (a) Three-dimensional isosurface of $\eta = 0.65$ in a shortened domain, starting from $\theta = 0°$ with outflow length equal to $2D$. (b) Two-dimensional isocontours of $\eta$ (top) in the symmetry plane for $\theta$ between 0° and 90° and (bottom) in the cross plane at $\theta = 15°$. The black arrows indicate the flow direction.

mechanism acts. This is defined as

$$\eta(\mathbf{x}) = \frac{\|\hat{\boldsymbol{u}}^{\dagger}(\mathbf{x})\|\,\|\hat{\boldsymbol{u}}(\mathbf{x})\|}{\int_{\Omega} \hat{\boldsymbol{u}}^{\dagger}(\mathbf{x})\hat{\boldsymbol{u}}'(\mathbf{x})\mathrm{d}\Omega}, \tag{11}$$

where $\Omega$ is the computational domain and $\|\cdot\|$ is the magnitude. The sensitivity map of the unstable eigenmode is shown in Fig. 9. The region of high sensitivity of the flow to localized feedback from the velocity field can be determined by analyzing the spatial distribution of the structural sensitivity function $\eta$. The results show that the significant values of $\eta$ are limited to the region located inside the bend, specifically on the outer wall and at an angular distance of approximately 15° from the inlet. This suggests that any modifications or perturbations to the flow in this area could have a considerable impact on the stability of the system. In particular, the function $\eta$ considers the feedback that triggers the self-sustained oscillations, making it valuable in identifying the region of the flow that operates as a wavemaker [49]. As described in Sec. II, the direct $\hat{\boldsymbol{u}}$ and adjoint $\hat{\boldsymbol{u}}^{\dagger}$ are computed onto different meshes. Therefore, for evaluating the expression Eq. (11), a spectral interpolation on a single mesh is required. Note that the $\eta$ calculation is extremely robust with respect to to the chosen mesh, even with a fairly coarse one.

The location of the wavemaker, which is found to be approximately in the middle of the strongest separation bubble, is in agreement with the findings by Lupi *et al.* [14] for the 90°-bend flow. This analysis confirms that the 90°- and 180°-bend pipe flow undergo the same instability mechanism. The origin of the unsteadiness of the flow can be traced back to the shear layer, with a feedback mechanism triggered by the presence of the recirculation bubble. This conclusion is further supported by previous studies on various flow cases, which have shown a clear correlation between the onset of instability and the presence of a separation bubble (see, e.g., Schlatter *et al.* [38], Hammond and Redekopp [50], Marino and Luchini [51]).

## VI. CONCLUSIONS AND OUTLOOK

This paper analyzes the global stability and structural sensitivity of spatially developing pipe flow with a 180°-bend and curvature $\delta = R/R_c = 1/3$. First, we extracted the base flow from nonlinear DNSs using SFD. Second, we evaluated the numerical solution of the linear direct and adjoint problems. Third, we employed the implicitly restarted Arnoldi method [41] to compute the eigenvalue spectrum to verify the presence of only one unstable eigenvalue. Eventually, to reveal the nature of the transition, the structural sensitivity map is evaluated.

Given the critical role that mesh plays in numerical studies of flow stability, the AMR technique is employed. Specifically, we adapted the AMR technique, previously used in the context of external turbulent flows [22,26], to the linear and nonlinear solver in the spectral-element code Nek5000. Unlike previous applications, where AMR was mainly utilized to reduce computational costs, the primary focus on the stability analysis was to detect and refine poorly resolved regions of the initial mesh. Indeed, these may have given rise to large numerical errors and potentially trigger flow instability. We thus used independent meshes for the direct and dual linear solutions as well as the nonlinear base flow. A reduction in the computational cost was also observed. Although it is not as substantial as in the case of turbulent flows, where a tenfold reduction in grid points was measured, it remains noteworthy, approximately around a factor of 3. Furthermore, as a future prospect, it could be beneficial to create separate meshes for each of the first $m$ eigenvalues in the Arnoldi method, especially when multiple unstable eigenvalues exist. However, this would require significant modifications to the solver with additional computational challenges. Nonetheless, as an initial step, we believe that this paper already yields promising and noteworthy results.

We started by performing nonlinear DNSs. Another study in the literature that investigates the transition in spatially developing 180°-bend pipe flow is Hashemi *et al.* [15]. However, this study does not perform an actual stability calculation and reports an exceedingly high Reynolds number. As previously mentioned, we retain that an inconsistent normalization was performed in that study using the centerline velocity instead of the declared bulk velocity. The actual global stability analysis confirms the nonlinear DNS findings: By linearly interpolating the growth rate values of the least stable mode at $\mathrm{Re}_b = 2500$ and $\mathrm{Re}_b = 2550$, we estimated the critical Reynolds number to be $\mathrm{Re}_{b,\mathrm{cr}} = 2528$. Thus, the Hopf bifurcation occurs at this Reynolds number, which is considerably lower than the critical Reynolds number for the corresponding flow in a torus ($\mathrm{Re}_{b,\mathrm{cr}} = 3290$; see Ref. [11]). The computation of the eigenvalue spectrum confirms the existence of only one pair of complex conjugate eigenvalues for the direct and dual operators, with a growth rate $\sigma = 0.0342$ and angular frequency $\omega = 1.462$. The latter corresponds to a Strouhal number $\mathrm{St} = 0.233$, in agreement with the oscillation of the separation bubbles at $\mathrm{Re}_b = 2550$ observed in the nonlinear simulations. The direct eigenmode is characterized by a small, closed ring-shaped structure near the outer wall in proximity to the bend inlet. This structure grows in amplitude as the streamwise distance increases downstream. On the other hand, the adjoint eigenmode is concentrated in the section upstream of the bend and close to the bend inlet. Due to the non-normality of the NS operator, the large spatial separation between the two modes makes it challenging to draw any conclusive insights into the instability origin by investigating them separately. Therefore, we conducted an analysis of the unstable eigenmode sensitivity to spatially localized velocity feedback [49]. The resulting sensitivity map revealed significant values on the outer wall inside the bend, approximately 15° downstream of the bend inlet.

We conclude that the instability is caused by the separation of the shear layer, where a recirculation bubble is present, in a similar way to the spatially developing 90°-bend pipe flow with equal curvature. Thus, it is likely that large bends (i.e., larger than 180°) would show the same instability behavior. For shorter bends (lower than 90°), the Hopf bifurcation needs to disappear when approaching a straight pipe. It would be interesting to identify the critical angle. Our findings suggest that it can be estimated to be approximately 20°, given the location of the wavemaker region. Regarding the further geometrical parameter, i.e., the curvature, based on the present results, it is argued that at higher curvatures $\delta$, the instability mechanism is very likely to be the same discussed

here due to the even stronger shear layers. A different scenario is expected for lower curvatures, where a subcritical transition to turbulence might occur, triggered by finite-amplitude perturbations, as in toroidal pipes [13]. That said, this paper also provides a comprehensive characterization of the steady base flow in the 180°-bend pipe flow using high-order spectrally accurate nonlinear DNSs. This finding is particularly significant as it can be utilized for fine-tuning more complex simulations, including those involving blood flow in the aorta.

## ACKNOWLEDGMENTS

Financial support provided by the Knut and Alice Wallenberg Foundation and the Swedish Research Council Grant No. 2017-04421 (VR) is gratefully acknowledged. The simulations were performed on resources provided by the Swedish National Infrastructure for Computing (SNIC) at the PDC (KTH Stockholm) and NSC (Linköping University).

The authors report no conflicts of interest.

[1] J. Eustice, Experiments on stream-line motion in curved pipes, Proc. R. Soc. Lond. A **85**, 119 (1911).
[2] W. R. Dean, Note on the motion of fluid in a curved pipe, Lond. Edinb. Dubl. Philos. Mag. J. Sci. **4**, 208 (1927).
[3] W. R. Dean, The streamline motion of fluid in a curved pipe, Lond. Edinb. Dubl. Philos. Mag. J. Sci. **5**, 673 (1928).
[4] S. A. Berger, L. Talbot, and L. S. Yao, Flow in curved pipes, Annu. Rev. Fluid Mech. **15**, 461 (1983).
[5] J. Eustice, Flow of water in curved pipes, Proc. R. Soc. Lond. A **84**, 107 (1910).
[6] G. I. Taylor, The criterion for turbulence in curved pipes, Proc. R. Soc. Lond. A **124**, 243 (1929).
[7] C. M. White, Streamline flow through curved pipes, Proc. R. Soc. Lond. A **123**, 645 (1929).
[8] K. Sreenivasan and P. Strykowski, Stabilization effects in flow through helically coiled pipes, Exp. Fluids **1**, 31 (1983).
[9] J. Kühnen, M. Holzner, B. Hof, and H. C. Kuhlmann, Experimental investigation of transitional flow in a toroidal pipe, J. Fluid Mech. **738**, 463 (2014).
[10] J. Kühnen, P. Braunshier, M. Schwegel, H. C. Kuhlmann, and B. Hof, Subcritical versus supercritical transition to turbulence in curved pipes, J. Fluid Mech. **770**, R3 (2015).
[11] J. Canton, P. Schlatter, and R. Örlü, Modal instability of the flow in a toroidal pipe, J. Fluid Mech. **792**, 894 (2016).
[12] J. Canton, R. Örlü, and P. Schlatter, Characterisation of the steady, laminar incompressible flow in toroidal pipes covering the entire curvature range, Int. J. Heat Fluid Flow **66**, 95 (2017).
[13] J. Canton, E. Rinaldi, R. Örlü, and P. Schlatter, Critical point for bifurcation cascades and featureless turbulence, Phys. Rev. Lett. **124**, 014501 (2020).
[14] V. Lupi, J. Canton, and P. Schlatter, Global stability analysis of a 90°-bend pipe flow, Int. J. Heat Fluid Flow **86**, 108742 (2020).
[15] A. Hashemi, P. F. Fischer, and F. Loth, Direct numerical simulation of transitional flow in a finite length curved pipe, J. Turbul. **19**, 664 (2018).
[16] J. N. Nordström, N. Nordin, and D. S. Henningson, The fringe region technique and the Fourier method used in the direct numerical simulation of spatially evolving viscous flows, SIAM J. Sci. Comput. **20**, 1365 (1999).
[17] P. F. Fischer, J. Lottes, and S. Kerkemeier, Nek5000: open source spectral element CFD solver, https://nek5000.mcs.anl.gov.
[18] A. T. Patera, A spectral element method for fluid dynamics: Laminar flow in a channel expansion, J. Comput. Phys. **54**, 468 (1984).
[19] J. Malm, P. Schlatter, P. F. Fischer, and D. S. Henningson, Stabilization of the spectral element method in convection dominated flows by recovery of skew-symmetry, J. Sci. Comp. **57**, 254 (2013).

[20] N. Offermans, Aspects of adaptive mesh refinement in the spectral element method, Ph.D. thesis, Royal Institute of Technology, KTH, 2019.
[21] N. Offermans, A. Peplinski, O. Marin, and P. Schlatter, Adaptive mesh refinement for steady flows in Nek5000, Comput. Fluids **197**, 104352 (2020).
[22] N. Offermans, D. Massaro, A. Peplinski, and P. Schlatter, Error-driven adaptive mesh refinement for unsteady turbulent flows in spectral-element simulations, Comput. Fluids **251**, 105736 (2023).
[23] D. Massaro, A. Peplinski, and P. Schlatter, Interface discontinuities in spectral-element simulations with adaptive mesh refinement, in *Spectral and High Order Methods for Partial Differential Equations ICOSAHOM 2020+1*, edited by J. M. Melenk, I. Perugia, J. Schöberl, and C. Schwab (Springer International Publishing, Cham, 2023), pp. 375–386.
[24] J. Slotnick, A. Khodadoust, J. Alonso, D. Darmofal, W. Gropp, E. Lurie, and D. Mavriplis, CFD Vision 2030 Study: A path to revolutionary computational aeroscience, Tech. Rep. No. NASA/CR-2014-218178, National Aeronautics and Space Administration, 2014.
[25] D. Massaro, A. Peplinski, and P. Schlatter, Direct numerical simulation of turbulent flow around 3D stepped cylinder with adaptive mesh refinement, in *Twelfth International Symposium on Turbulence and Shear Flow Phenomena (TSFP12)* (2022), http://www.tsfp-conference.org/proceedings/proceedings-of-tsfp-12-2022-osaka.html.
[26] D. Massaro, A. Peplinski, and P. Schlatter, Coherent structures in the turbulent stepped cylinder flow at $\mathrm{Re}_D = 5000$, Int. J. Heat Fluid Flow **102**, 109144 (2023).
[27] D. Massaro, V. Lupi, A. Peplinski, and P. Schlatter, Adaptive mesh refinement for global stability analysis of transitional flows, arXiv:2309.10574.
[28] C. Mavriplis, Nonconforming discretizations and a posteriori error estimators for adaptive spectral element techniques, Ph.D. thesis, MIT, 1989.
[29] C. Burstedde, L. C. Wilcox, and O. Ghattas, p4est: Scalable algorithms for parallel adaptive mesh refinement on forests and octrees, SIAM J. Sci. Comput. **33**, 1103 (2011).
[30] G. W. Kruse, Parallel nonconforming spectral element solution of the incompressible Navier-Stokes equations in three dimensions, Ph.D. thesis, Brown University, 1997.
[31] A. Peplinski, N. Offermans, P. F. Fischer, and P. Schlatter, Non-conforming elements in Nek5000: Pressure preconditioning and parallel performance, in *Spectral and High Order Methods for Partial Differential Equations ICOSAHOM 2018*, edited by S. J. Sherwin, D. Moxey, J. Peiró, P. E. Vincent, and C. Schwab (Springer International Publishing, Cham, 2020), pp. 599–609.
[32] N. Offermans, O. Marin, M. Schanen, J. Gong, P. Fischer, P. Schlatter, A. Obabko, A. Peplinski, M. Hutchinson, and E. Merzari, On the strong scaling of the spectral element solver Nek5000 on petascale systems, in *Proceedings of the Exascale Applications and Software Conference 2016* (Association for Computing Machinery, New York, 2016).
[33] A. Noorani, A. Peplinski, and P. Schlatter, Informal introduction to program structure of spectral interpolation in Nek5000, Tech. Rep., KTH Royal Institute of Technology, 2015.
[34] D. Massaro, A. Peplinski, and P. Schlatter, The flow around a stepped cylinder with turbulent wake and stable shear layer, J. Fluid Mechanics (to be published).
[35] E. Åkervik, L. Brandt, D. S. Henningson, J. Hœpffner, O. Marxen, and P. Schlatter, Steady solutions of the Navier-Stokes equations by selective frequency damping, Phys. Fluids **18**, 068102 (2006).
[36] S. Strogatz, *Nonlinear Dynamics and Chaos: With Applications to Physics, Biology, Chemistry, and Engineering* (Perseus Books Group, 2018).
[37] L. S. Tuckerman and D. Barkley, Bifurcation analysis for timesteppers, in *Numerical Methods for Bifurcation Problems and Large-Scale Dynamical Systems*, edited by E. Doedel and L. S. Tuckerman (Springer, New York, 2000), pp. 453–466.
[38] P. Schlatter, S. Bagheri, and D. S. Henningson, Self-sustained global oscillations in a jet in crossflow, Theor. Comput. Fluid Dyn. **25**, 129 (2011).
[39] S. Bagheri, E. Åkervik, L. Brandt, and D. S. Henningson, Matrix-free methods for the stability and control of boundary layers, AIAA J. **47**, 1057 (2009).

[40] D. C. Sorensen, Implicit application of polynomial filters in a $k$-step Arnoldi method, SIAM J. Matrix Anal. Appl. **13**, 357 (1992).
[41] R. B. Lehoucq, D. C. Sorensen, and C. Yang, *ARPACK Users' Guide: Solution of Large-Scale Eigenvalue Problems with Implicitly Restarted Arnoldi Methods* (Society for Industrial and Applied Mathematics, 1998).
[42] A. Peplinski, P. Schlatter, and D. S. Henningson, Global stability and optimal perturbation for a jet in cross-flow, Eur. J. Mech. B Fluids **49**, 438 (2015).
[43] D. Massaro, A. Peplinski, R. Stanly, S. Mirzareza, V. Lupi, T. Mukha, and P. Schlatter, A comprehensive framework to enhance numerical simulations in the spectral-element code Nek5000 (unpublished).
[44] J. M. Chomaz, Global instabilities in spatially developing flows: Non-normality and nonlinearity, Annu. Rev. Fluid Mech. **37**, 357 (2005).
[45] L. Trefethen, A. Trefethen, S. Reddy, and T. Driscoll, Hydrodynamic stability without eigenvalues, Science **261**, 578 (1993).
[46] P. J. Schmid and D. S. Henningson, *Stability and Transition in Shear Flows*, Applied Mathematical Sciences (AMS) Vol. 142 (Springer, New York, 2001).
[47] J. M. Chomaz, P. Huerre, and L. G. Redekopp, A frequency selection criterion in spatially-developing flows, Stu. App. Math. **84**, 119 (1991).
[48] P. Monkewitz, P. Huerre, and J. M. Chomaz, Global linear stability analysis of weakly non-parallel shear flows, J. Fluid Mech. **251**, 1 (1993).
[49] F. Giannetti and P. Luchini, Structural sensitivity of the first instability of the cylinder wake, J. Fluid Mech. **581**, 167 (2007).
[50] D. A. Hammond and L. G. Redekopp, Local and global instability properties of separation bubbles, Eur. J. Mech. B Fluids **17**, 145 (1998).
[51] L. Marino and P. Luchini, Adjoint analysis of the flow over a forward-facing step, Theor. Comput. Fluid Dyn. **23**, 37 (2009).